



OPEN

Four dimensional-scanning transmission electron microscopy study on relationship between crystallographic orientation and spontaneous polarization in epitaxial BiFeO₃

In-Tae Bae¹✉, Brendan Foran¹ & Hanjong Paik^{2,3}

Spontaneous polarization and crystallographic orientations within ferroelectric domains are investigated using an epitaxially grown BiFeO₃ thin film under bi-axial tensile strain. Four dimensional-scanning transmission electron microscopy (4D-STEM) and atomic resolution STEM techniques revealed that the tensile strain applied is not enough to cause breakdown of equilibrium BiFeO₃ symmetry (rhombohedral with space group: $R\bar{3}c$). 4D-STEM data exhibit two types of BiFeO₃ ferroelectric domains: one with projected polarization vector possessing out-of-plane component only, and the other with that consisting of both in-plane and out-of-plane components. For domains with only out-of-plane polarization, convergent beam electron diffraction (CBED) patterns exhibit “extra” Bragg’s reflections (compared to CBED of cubic-perovskite) that indicate rhombohedral symmetry. In addition, beam damage effects on ferroelectric property measurements were investigated by systematically changing electron energy from 60 to 300 keV.

BiFeO₃ (BFO) is the only known material that shows two primary ferroic orders, i.e., ferroelectricity and antiferromagnetism, simultaneously above room temperature^{1,2}. It has been intensively studied for a couple of decades to test the feasibility of electric field control of magnetism, which implies ground-breaking potential for electronics applications such as multiply controlled devices^{3–5}. The primary method used to grow BFO is epitaxy via pulsed laser deposition, molecular beam epitaxy, or ultra-high vacuum sputtering. The technological advantage of epitaxial growth is to allow for modification of BFO characteristics by imparting elastic strain (caused by lattice mismatch with substrate material) without causing lattice defects such as misfit dislocations⁶. Since crystal symmetry information is closely associated with properties, such as spontaneous polarization, understanding of the relationships between crystal symmetry, orientation and spontaneous polarization is of great technological importance.

A variety of metastable BFO phases have been identified, experimentally and theoretically, as dependent on: (1) the amount of elastic strain and (2) type of elastic strains, i.e., either compressive or tensile. It is worth noting that the magnitudes of spontaneous polarization reported for metastable BFO phases found experimentally were similar to that of equilibrium BFO (i.e., 90–100 $\mu\text{C}/\text{cm}^2$). This is in disagreement with higher values predicted by theoretical calculations^{7,8}.

While some of the metastable BFO phases are reported with complete symmetry information such as space group, lattice parameter, and basis atom locations, others are simply based on lattice parameter distortions measured by X-ray diffraction and include no such information^{7–18}. Most of the previously reported metastable BFO phases have used a pseudocubic (*pc*) notation for equilibrium BFO with a lattice parameter of ~ 0.396 nm to evaluate the elastic strain. However, the *pc* notation of equilibrium BFO disregards two crucial rhombohedral characteristics, i.e., (1) $\sim 0.5^\circ$ rhombohedral distortion and (2) basis atom location shifts caused by oxygen

¹Microelectronics Technology Department, The Aerospace Corporation, El Segundo, CA 90245, USA. ²School of Electrical and Computer Engineering, University of Oklahoma, Norman, OK 73019, USA. ³Center for Quantum Research and Technology, University of Oklahoma, Norman, OK 73019, USA. ✉email: intae.bae@aero.org

octahedron rotation in equilibrium BFO; thus the *pc* approximation does not represent *true* symmetry in equilibrium BFO^{19–21}.

Most of the experimentally found metastable BFO phase identifications were made based on small distortions relative to *pc* notation-approximated equilibrium BFO unit cell. Few of these studies have shown electron diffraction patterns from metastable BFO phases with appropriate detailed analysis to effectively evaluate symmetry utilizing unit cell distortions with accurate *basis atom* positions. For example, nano-beam electron diffraction patterns combined with structure factor calculation (that makes use of *true* equilibrium BFO symmetry using *hexagonal* notation) unambiguously demonstrated the existence of Bragg's reflections at Q (scattering vector) $\approx 4.18 \text{ nm}^{-1}$ specifically tied to a rhombohedral distortion, i.e., oxygen octahedral rotation, in equilibrium BFO phase²¹. While the Bragg's reflections can be readily used to distinguish rhombohedral BFO from other metastable BFO phases (owing to their exclusive association with rhombohedral BFO), only a few studies implementing the Bragg's reflections have been reported^{22–25}. Thus, the relationship between the crystal symmetries of metastable BFO phases and their spontaneous polarization property remain debated.

In this study, four dimensional-scanning transmission electron microscopy (4D-STEM) technique^{26,27} is applied to an epitaxial BFO film designed to be under tensile strain using PrScO_3 (PSO) single crystal to investigate: (1) crystal symmetry within BFO film, (2) ferroelectric domain structure within BFO film in terms of the relationship between spontaneous polarization and crystallographic orientations, and (3) beam-damage effects on measured ferroelectric domain structure.

Results and discussion

Figure 1a shows a high angle annular dark field (HAADF)-STEM image of the BFO films grown on (101)_o PSO substrate (space group: $Pnma$, $a = 0.5780 \text{ nm}$, $b = 0.8025 \text{ nm}$, $c = 0.5608 \text{ nm}$, $\alpha = \beta = \gamma = 90^\circ$) along $[\bar{1}11]_o$ (subscript “o” stands for orthorhombic notation) zone axis using 120 keV electron probe²⁸. ~20 nm BFO epitaxial film shows up brighter than underlying PSO substrate because Bi atom within BFO, which is heavier than Pr and Sc in PSO, provides more signals to the HAADF detector located at the collection semi-angle of 80–100 mrad²⁹. A green rectangle in Fig. 1a indicates the area where a 4D-STEM data set, two probe-scanning dimensions in real space and two momentum dimensions in reciprocal space, were acquired using 120 keV electron probe as shown in Fig. 1b–e. Figure 1b shows an example of a convergent beam electron diffraction (CBED) pattern that was collected from each scanning position in Fig. 1c–e. While 4D-STEM data acquisition with sub-angstrom aberration corrected electron probes is known to be advantageous to visualize the potential gradient across single atomic columns and the nuclear charge in GaN and SrTiO_3 ^{30–32}, sub-angstrom electron probes with large convergence angles cause Bragg's reflections in CBED patterns to overlap, which complicates measurement of

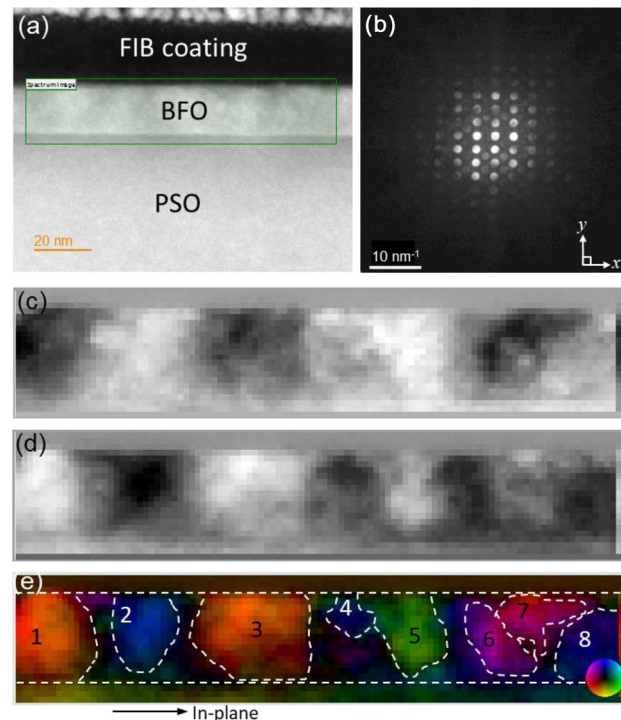


Figure 1. (a) A cross-sectional HAADF-STEM image of epitaxial BFO grown on PSO along $[\bar{1}11]_o$ zone axis using 120 keV electron probe (b) an example of CBED pattern from BFO, (c) the measured shift in zeroth order diffraction disks in CBED patterns along x direction, i.e., dx , (d) the measured shift in zeroth order diffraction disks in CBED patterns along y direction, i.e., dy , (e) vector displacement map with a color wheel as an inset bottom right corner. Ferroelectric domains are denoted by white-dashed lines with numbers.

long range electric fields arising from ionicity because 4D-STEM signal is dominated by nuclear potential^[33,34]. Thus, a small convergence semi-angle of ~ 1.26 mrad is used to prevent Bragg's reflection overlaps as shown in Fig. 1b. The spontaneous polarization orientations within BFO domains were determined by analysis of zeroth order CBED pattern shift along two orthogonal directions, i.e., x and y , as denoted in Fig. 1b. These shifts are known to occur due to the deflection of the incident electron beam by average electric field over unit cell in ferroelectric materials, whereas asymmetric intensities in conjugate disks resulting from Friedel's law breakage allows for polarity field measurement^[26,27,33,34]. While no obvious contrast resulting from spontaneous polarization is seen from BFO layer in HAADF-STEM image (see Fig. 1a), areas with distinctively bright and dark contrasts are seen in Fig. 1c and d. The color-coded vector displacement map, based on Fig. 1c and d, is shown in Fig. 1e. Note that the intensity scales to the magnitude of the vector field and the color represents its orientation as shown by the color wheel at bottom-right corner. Ferroelectric domains with sizes ranging from ~ 10 to ~ 25 nm are clearly identified. Table 1 summarizes the distribution of spontaneous polarization orientations in each domain with respect to the in-plane orientation denoted in Fig. 1e. Note that the polarization angles measured are based on projection along $[\bar{1}11]_0$ PSO orientation. The mean and standard deviation are based on 10 pixels from the central area of each ferroelectric domain. It is worth noting that domains 2, 4, and 8 possess only an out-of-plane component of polarization with polarization angles $\sim -90^\circ$. All other domains have both of out-of-plane and in-plane polarization components, i.e., their polarization angles $\neq \pm 90^\circ$.

Prior to further discussion on the relationship between spontaneous polarization and crystallographic orientations, crystal symmetry within the BFO films needs to be identified. CBED patterns from domains 1 through 4, extracted from 4D-STEM data set, are shown in Fig. 2. While Fig. 2a-d all exhibit fundamental Bragg's reflections,

Domain	Angle with respect to in-plane orientation (deg.)	
	Mean	Standard deviation
1	135.2	3.5
2	-87.7	4.8
3	133.4	3.4
4	-90.2	4.8
5	46.7	3.8
6	-154.9	6.5
7	155.2	9.1
8	-90.5	3.8

Table 1. Summary of the spontaneous polarization angles, i.e., mean and standard deviation, with respect to the *in-plane* orientation denoted as an arrow in Fig. 1e.

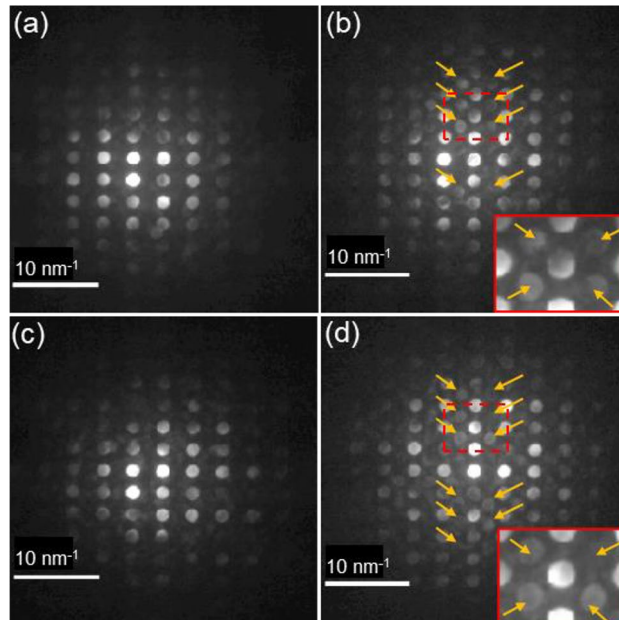


Figure 2. CBED patterns acquired from domains 1 (a), 2 (b), 3 (c), and 4 (d) using 120 keV electron probe. Extra Bragg's reflections are denoted by orange arrows in (b) and (d). The two boxed areas in red in (b) and (d) are magnified as insets at the bottom-right corner, respectively.

extra Bragg's reflections (denoted by orange arrows) can be observed in Fig. 2b and d only. The two boxed areas in red in Fig. 2b and d are magnified as insets at the bottom-right corner, respectively. This clearly indicates that while Fig. 2a and c correspond to $[110]_h$ (subscript "h" denotes three index hexagonal notation) zone axes of rhombohedral BFO, i.e., equilibrium BFO, Fig. 2b and d match $[\bar{1}11]_h$ zone axis of rhombohedral BFO (see Table S1 for h to pc notation conversion). This result is in good agreement with a recent work that performed nano-beam electron diffraction analysis for BFO grown on PSO substrate²¹. Note that $[110]_h$ and $[\bar{1}11]_h$ zone axes found in the present work are crystallographically equivalent to $[0\bar{1}0]_h$ and $[211]_h$ zone axes found in the recent work²¹, respectively, as the angles between the corresponding orientations are 120° and the CBED patterns of the corresponding orientations are identical (see Figure S1). In addition, the work showed that the extra Bragg's reflections shown in Fig. 2b and d are the result of oxygen octahedral rotation occurring in rhombohedral BFO (space group: $R\bar{3}c$; lattice parameter: $a = 0.5678$ nm, and $c = 1.3982$ nm) by demonstrating that the electron diffraction simulation of pc notation-approximated BFO (space group: $Pm\bar{3}m$; lattice parameter $a = 0.396$ nm) that possesses no oxygen octahedral rotation exhibits no such extra Bragg's reflections²¹.

Since local electronic structure in O (oxygen) K -edge in BFO is known to be sensitive to local bonding and geometry¹⁸, an electron energy loss spectrum (EELS) is acquired from the BFO film with ~ 1.0 eV FWHM energy resolution (see Fig. 3). The O K -edge spectral features can be discussed for two regions, as defined by the labels A, A' and B, B' as shown in Fig. 3. Peaks A and A' are readily attributed to hybridization between O $2p$ and Fe $3d$ states and a transition between O $2p$ and Bi $5d$ (or $6d$) states, respectively^{35–37}. Peaks B and B' are associated with hybridization between O $2p$ and Fe $4sp$ states in bulk and thin BFO^{35,36,38}. The relative intensities of A and A', and of B and B' are in good agreement with those for bulk and thin film rhombohedral BFO, where the bonding geometry between Fe and O atoms is octahedral^{23,35–37}. Note that these are in disagreement with metastable BFO phases that show the relative intensity inversion for B and B'^{17,18,36}. Accordingly, the EELS result on O K -edge film is consistent with the rhombohedral symmetry found from CBED patterns in Fig. 2.

Figure 4 shows two atomic resolution HAADF-STEM images for the BFO/PSO interface [recorded at domains 1 and 2, respectively, of Fig. 1e] to investigate strain within BFO film which is expected from lattice misfit ($\sim 1.5\%$) with PSO^{6,21,39}. The PSO lattice spacing along the in-plane orientation, i.e., $(\bar{1}21)_o$, is commensurate with that of the BFO, i.e., $(\bar{1}14)_h$, in domain 1 (see Fig. 4a) and $(110)_h$ in domain 2 (see Fig. 4b), with no sign of misfit dislocations despite $\sim 1.5\%$ of lattice misfit. Since misfit dislocations, known to relax elastic strain when the density is higher than a threshold value, are not found, the elastic strain resulting from $\sim 1.5\%$ of lattice misfit with PSO is thought to be maintained within BFO film. Fast Fourier transform (FFT) patterns from domains 1 and 2 (see insets in Fig. 4a and b) show the same characteristics as found in CBED patterns, i.e., extra Bragg's reflections (denoted by orange arrows in the inset of Fig. 4b) were found for domain 2 only. Thus, the result in FFT analysis of atomic resolution HAADF-STEM data is consistent with that of CBED patterns.

The combined evidence of (1) rhombohedral symmetry (shown in Figs. 1, 2 and 3) and (2) $\sim 1.5\%$ tensile elastic strain (shown in Fig. 4), suggests that this level of strain falls below the threshold for equilibrium symmetry breakdown in this epitaxial BFO film. This result agrees with prior structural flexibility in rhombohedral BFO discussed previously in terms of: (1) a small perovskite tolerance factor (~ 0.88) allowing for large degree of rotation and/or tilting of oxygen octahedra⁴⁰, (2) variation in experimentally found lattice parameters for bulk rhombohedral BFO (i.e., $\sim 0.82\%$ in a and $\sim 0.71\%$ in c in hexagonal notation⁴¹), and (3) availability of multiple meta stable phases^{7,8}.

Let us turn our attention to the relationship between the spontaneous polarization orientations found in ferroelectric domains and their crystallographic orientations. Based on the results found in Figs. 1 and 2, an atomic model is constructed as shown in Fig. 5. Note that *no tensile strain* is assumed within BFO ferroelectric domains. Figure 5a shows that the *unstrained* interplanar distances between domains 1 and 2 are the same along out-of-plane [see $(11\bar{2})_h$ in domains 1 and 2] indicating this interface [see dotted line in Fig. 5a] shows no misfit strain. Note that the HAADF-STEM image showed no distinctive contrast across this interface because of: (1) no misfit stain field and (2) the close relationship of the projected crystal structures in these two different

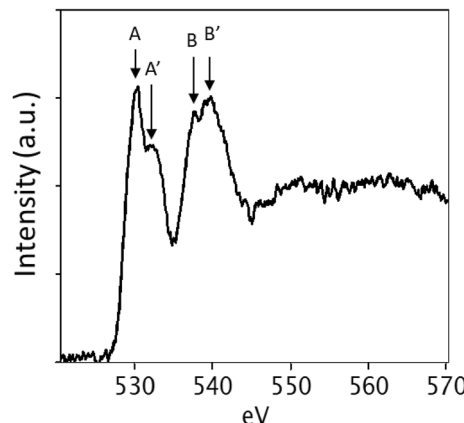


Figure 3. An EELS on O K -edge from BFO film using 120 keV electron probe with ~ 1.0 eV energy resolution.

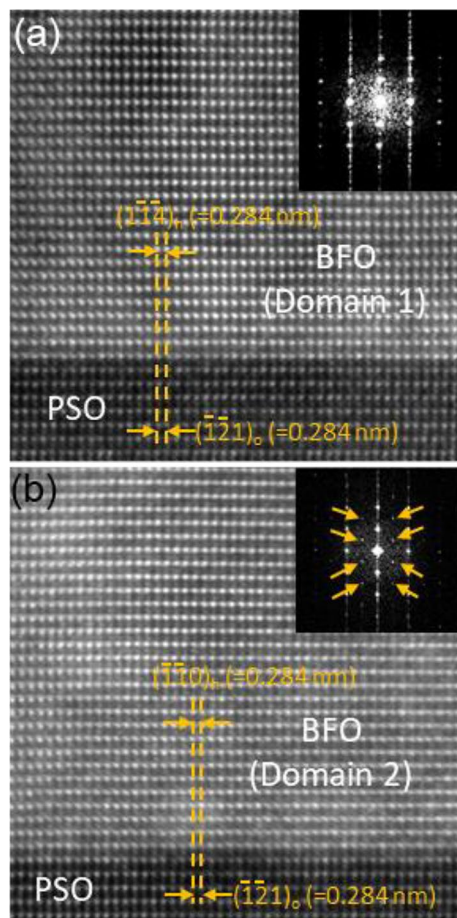


Figure 4. (a) Atomic resolution HAADF-STEM images from (a) BFO domain 1/PSO and (b) BFO domain 2/PSO interfaces along PSO $[\bar{1}11]_h$ zone axis. The interplanar distances of BFO I and BFO II along in-plane orientation are the same as those of PSO with no sign of misfit dislocations at the interfaces. FFT patterns from domains 1 and 2 are shown as insets at the top-right corner in (a) and (b), respectively, with extra Bragg's reflections from domain 2 denoted with orange arrows.

orientations. The differences in these crystal orientations are subtle and are not well distinguished when a *pc* notation is used to describe the equilibrium BFO lattice. Figure 5b and c show the rhombohedral BFO unit cell in hexagonal notation with zone axes aligned along $[110]_h$ (for domain 1) and $[\bar{1}11]_h$ (for domain 2), respectively. The spontaneous polarization orientations, i.e., $[001]_h$ orientation ($=[111]_{pc}$), are denoted with the arrows in blue. The basal plane, i.e., $(001)_h$ plane ($=[(111)_{pc}$ plane]), is also denoted in blue in each figure. Note that this plane in Fig. 5b is near perpendicular to the plane of the page and thus is almost hidden. The spontaneous polarization angles are calculated to be $\sim 144^\circ$ for domain 1 and $\sim -90^\circ$ for domain 2 with respect to in-plane orientation. While the $\sim 144^\circ$ value for domain 1 is $\sim 9^\circ$ from $\sim 135.2^\circ$ measured by 4D-STEM, the $\sim -90^\circ$ value for domain 2 matches more closely to the $\sim -87.7^\circ$ measured by 4D-STEM (see Table 1). Elastic strain in epitaxially grown BFO is known to cause spontaneous polarization orientation to change within $(110)_{pc}$ plane from the calculated angles of $\sim 144^\circ$ and $\sim -90^\circ$ based on *unstrained* BFO^{39,42}. Besides, polarity effect (showing up with asymmetric intensities in conjugate disks resulting from Friedel's law breakage) could contribute the spontaneous polarization orientation change. Note that $(110)_{pc}$ plane in Fig. 5b, i.e., domain 1, is parallel to the plane of the page whereas that in Fig. 5c, i.e., domain 2, is perpendicular to the plane of page. Thus, the polarization rotation caused by $\sim 1.5\%$ tensile strain is more readily measured in domain 1 than in domain 2. Based on the results in Figs. 1, 2 and 5, three dimensional polarization vectors for domains 1 and 2 are schematically drawn in Figure S2. Both of polarization vectors run along either of PSO diagonal orientations with $45.2 \pm 3.5^\circ$ off the BFO film surface in domain 1 (see Fig. S2a) and $35.6 \pm \text{dev}^\circ$ off the BFO film surface in domain 2 (see Fig. S2b). Note that while $45.2 \pm 3.5^\circ$ in domain 1 is based on 4D-STEM measurement, $35.6 \pm \text{dev}^\circ$ is an assumption defined by the sum of theoretical value of 35.6° for unstrained BFO⁴³ and (2) polarization vector change (dev.) owing to the tensile strain caused by PSO substrate. A recent aberration corrected TEM work on an epitaxial BFO film grown on PSO substrate revealed that while 70° ferroelectric domain wall consists of polarization components of both in-plane and out-of-plane orientations, 180° domain wall is comprised of out-of-plane polarization component only⁴⁴. Note that 70° and 180° represent the angles between two polarization vectors across domains. Since the projection orientation of BFO ferroelectric domain in the report is along $[110]_{pc}$ orientation, which is equivalent

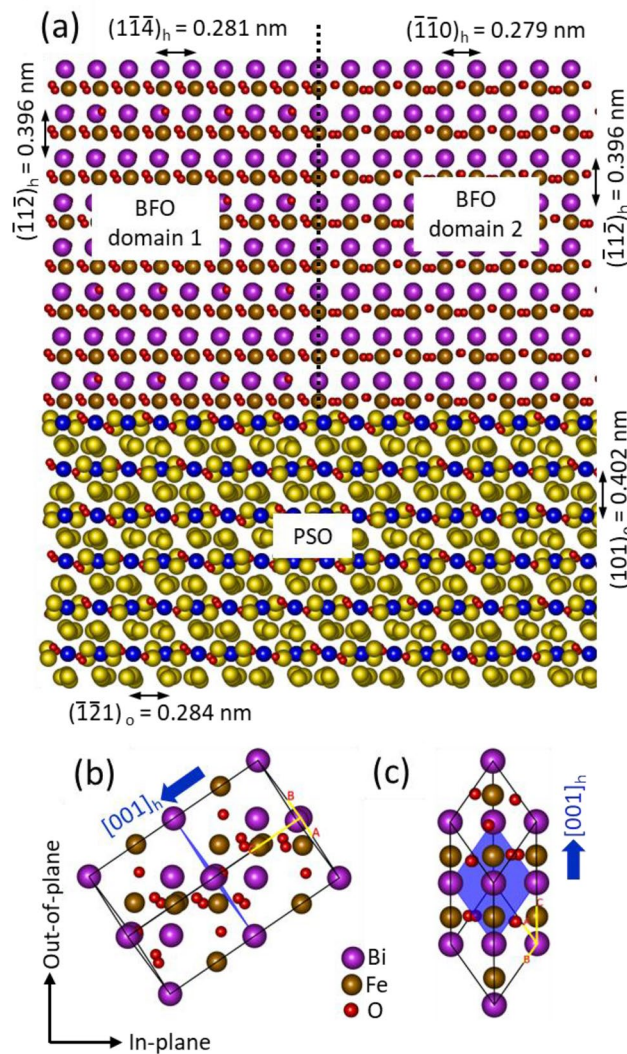


Figure 5. (a) Atomic model showing the epitaxial relationship between BFO domains 1 and 2 with respect to PSO substrate. Note that the out-of-plane interplanar distances between the two domains are identical. Spontaneous polarization orientations in BFO domains 1 (b) and 2 (c) are shown with blue arrows. Note that the BFO unit cell is projected along the corresponding zone axes of each BFO domain, i.e., $[110]_h$ for domain 1 and $[\bar{1}11]_h$ for domain 2. $(001)_h$ plane in each BFO domain is denoted in blue with the BFO unit cell.

to $[110]_h$ (for domain 1) and $[\bar{1}11]_h$ (for domain 2) in the current work, the conclusion in the prior report is consistent with the current one based on Figs. 1, 2 and 5.

Note that while the CBED pattern from domain 1 shows no extra Bragg's reflections (see Fig. 1a), that from domain 2 exhibits the extra Bragg's reflection (see Fig. 1b). Thus, the ferroelectric domain with no extra Bragg's reflections has spontaneous polarization orientation with both in-plane and out-of-plane components, whereas the one exhibiting extra Bragg's reflections possesses only an out-of-plane polarization component. This indicates that polarization orientation within BFO ferroelectric domains can be identified by the existence of extra Bragg's reflections in CBED pattern from BFO ferroelectric domain.

To investigate probe-beam damage effect on ferroelectric domain, 4D-STEM data were acquired at 60 and 300 keV as shown in Figs. 6 and 7. Figures 6a and 7a are the HAADF images, acquired from the *same* area as in Fig. 1a, at each keV, showing no sign of contrast that could be associated with ferroelectric domains. The examples of CBED pattern obtained at each keV are shown in Figs. 6b and 7b. Note that Bragg's reflections in the CBED patterns separate related to convergence angle adjustment (i.e., ~ 5.25 mrad for 60 keV and ~ 1.84 mrad for 300 keV). The color-coded vector displacement maps at each keV, based on shifts in zeroth order diffraction disks in CBED patterns (see Fig. 6c, d for 60 keV and Fig. 7c and d for 300 keV) are shown in Figs. 6e and 7e. Note that the intensity scales to the magnitude of the vector field and the color represents its orientation as shown by the color wheel at bottom-right corner in each figure. It can be readily noticed that while the shapes and colors of ferroelectric domains in Fig. 6e are comparable to those in Fig. 1e, those of ferroelectric domains in Fig. 7e are different than those in Fig. 1e in terms of domain morphology and colors, i.e., polarization orientations. In particular, the bottom quarter of BFO layer shows low signal/noise (S/N) ratio in Fig. 7e indicating that while

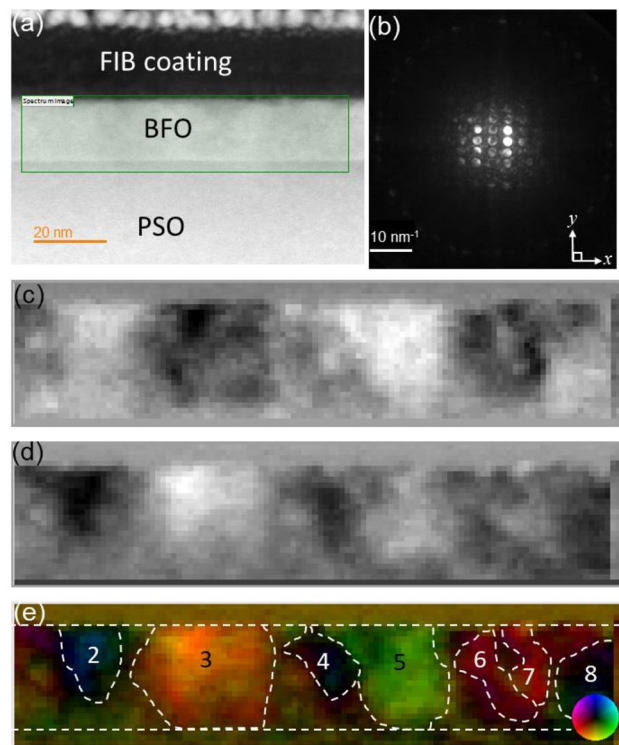


Figure 6. (a) A cross-sectional HAADF-STEM image of epitaxial BFO grown on PSO along $[\bar{1}11]_0$ zone axis using 60 keV electron probe, (b) an example of CBED pattern from BFO, (c) the measured shift in zeroth order diffraction disks in CBED patterns along x direction, i.e., dx , (d) the measured shift in zeroth order diffraction disks in CBED patterns along y direction, i.e., dy , (e) Vector displacement map with a color wheel as an inset bottom right corner. Ferroelectric domains are denoted by white-dashed lines with numbers.

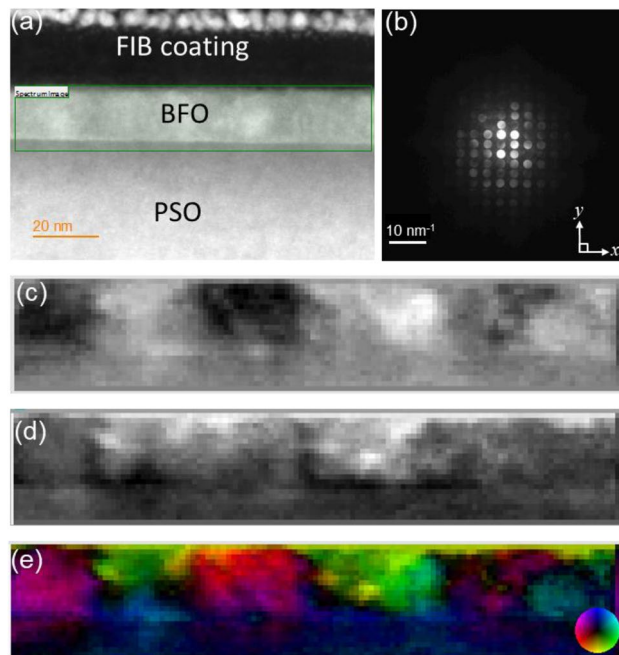


Figure 7. (a) A cross-sectional HAADF-STEM image of epitaxial BFO grown on PSO along $[\bar{1}11]_0$ zone axis using 300 keV electron probe, (b) an example of CBED pattern from BFO, (c) the measured shift in zeroth order diffraction disks in CBED patterns along x direction, i.e., dx , (d) the measured shift in zeroth order diffraction disks in CBED patterns along y direction, i.e., dy , (e) Vector displacement map with a color wheel as an inset bottom right corner.

120 and 60 keV probe energies induced no noticeable beam-damage, the 300 keV probe energy damaged BFO ferroelectric domain ordering. It is well known that high energy electron beams may cause both ionization and displacement damages. Since ionization damage decreases with increasing electron acceleration voltage^{45,46}, the beam damage found at 300 keV is most likely attributed to displacement damage. When incident electron provides recoil energy greater than threshold displacement energy, E_d , of each constituent atoms within target material, point defects, such as Frenkel pairs are introduced by knocked-on atoms. The maximum recoil energy, T_m , that an incident electron transfers to constituent atoms in target material is given by⁴⁶:

$$T_m = 2E(E + 2m_0c^2)/Mc^2$$
, where E is the energy of incident electron, m_0 the rest mass of electron, c the velocity of light, and M the mass of the displaced atom. Although E_d necessary to create knock-on damage and make stable point defects (such as Frenkel pair) have not yet been determined for BFO, ~ 25 eV was proposed as a general guideline of threshold displacement energy⁴⁷. Calculated T_m for Bi, Fe and O atoms at 60, 120, and 300 keV are summarized in Table 2. While most of the T_m values are less than ~ 25 eV of the suggested E_d , the T_m of ~ 53.2 eV found for O atoms at 300 keV is significantly greater than the suggested E_d indicating that 300 keV electrons likely cause displacement damage in BFO through accumulation of O vacancies and interstitials. Previous theoretical studies discussed that O-poor conditions provide fully ionized oxygen vacancies which pair with cation atom to lead to local ferroelectric polarization called imprint effect which disturb spontaneous polarization within BFO^{48,49}.

Since electron beam capable of providing T_m that is greater than E_d to constituent atoms is known to knock-off the atoms from exit surface of the sample through displacement damage process^{50,51}, it is reasonably assumed that 300 keV electron probe used in the current study can cause displacement damage leading to O-poor condition within BFO leading to disturb spontaneous polarization through imprint effect. This can be the reason of modified shapes and colors with low S/N ratio area found in measured ferroelectric domains by 300 keV electron probe as shown in Fig. 7e.

Summary

4D-STEM technique was applied to an epitaxial BFO film engineered to be under ~ 1.5 % of bi-axial tensile strain using PSO single crystal substrate. Our key results include:

- (1) Color-coded vector displacement map derived from 4D-STEM center of mass deflection measurements identified BFO ferroelectric domains with sizes ranging from ~ 10 to ~ 25 nm. Two types of ferroelectric domains were observed, i.e., one with both in-plane and out-of-plane polarization components and the other with an out-of-plane polarization only.
- (2) Further comparison with CBED patterns acquired from the ferroelectric domains indicates correlation between extra Bragg's reflections and the polarization component characteristic, i.e. extra Bragg' reflections indicate out-of-plane polarization only; no extra Bragg's reflection leads to both in-plane and out-of-plane polarization components within BFO ferroelectric domains.
- (3) While atomic resolution HAADF images indicates ~ 1.5% biaxial tensile strain within BFO film elastically, CBED and EELS analyses suggest that the strain is not enough to cause rhombohedral symmetry breakdown within BFO film.
- (4) Comparison of 4D-STEM data recorded at different incident electron probe energies (60, 120, and 300 keV tested) identified that displacement damage observed at 300 keV could reduce (and modify) measurable ferroelectric property within BFO film through possibly O vacancy formation.

Methods

An epitaxial BFO film of ~ 20 nm was grown on a (101)₀ PSO substrate using molecular beam epitaxy in PAPA-DIM facility at Cornell University. The cross-sectional sample preparation for 4D-STEM measurement was performed using a Ga ion Dual beam focused ion beam, Thermo Fisher Helios 600. Ga ion energy was gradually decreased from 30 to 2 kV to minimize ion beam induced damage. A Thermo Fisher Titan Themis G2 300 equipped with a probe corrector was used for 4D-STEM data acquisition at acceleration voltages ranging from 60 to 300 keV. The convergence semi-angles of electron probe were adjusted between ~ 1.25 to ~ 5.25 mrad to separate Bragg's reflections in CBED patterns. CBED patterns were calibrated using [202] and [202] Bragg's reflections of PSO substrate. Two different values of camera length, i.e., 160 (for 60 kV) and 300 (for 120 and 300 kV) mm were used to collect large spatial frequency (up to ~ 20 nm⁻¹) information in CBED patterns. A Gatan OneViewTM CMOS camera with readout binned to 512 × 512 pixels was used to collect diffraction data for 4D STEM. HAADF-STEM images and 4D-STEM were collected with ~ 176° image rotation with respect to CBED

Electron energy (keV)	Maximum recoil energy, T_m , (eV)		
	Bi	Fe	O
60	~ 0.7	~ 2.5	~ 8.7
120	~ 1.4	~ 5.3	~ 18.4
300	~ 4.1	~ 15.2	~ 53.2

Table 2. Summary of maximum recoil energy, T_m , for Bi, Fe, and O atoms against electron probe energy ranging from 60 to 300 keV.

patterns. The Gatan Microscopy Suite software was used to analyze 4D STEM data using a center of mass method that fits shifts across the full CBED pattern at each pixel position. The image rotation of $\sim 176^\circ$ was compensated before center of mass data process. A Gatan Image Filter (GIF) Quantum was used to acquire EELS data.

Data availability

All data generated or analyzed during this study are included in the published article. In case, one wished to consult further information, it will be made available through the corresponding author on reasonable request.

Received: 7 May 2024; Accepted: 1 July 2024

Published online: 05 July 2024

References

1. Kiselev, S. V., Ozerov, R. P. & Zhdanov, G. S. Detection of magnetic order in ferroelectric BiFeO_3 by neutron diffraction. *Soviet Phys. Doklady* **7**, 742–744 (1963).
2. Smolenskii, G. A. & Chupis, I. E. Segnetomagnetics. *Uspekhi Fiz. Nauk* **137**, 415–448. <https://doi.org/10.3367/UFNr.0137.198207b.0415> (1982).
3. Spaldin, N. A. & Fiebig, M. The renaissance of magnetoelectric multiferroics. *Science* **309**, 391–392. <https://doi.org/10.1126/science.1113357> (2005).
4. Eerenstein, W., Mathur, N. D. & Scott, J. F. Multiferroic and magnetoelectric materials. *Nature* **442**, 759–765. <https://doi.org/10.1038/nature05023> (2006).
5. Zhao, T. *et al.* Electrical control of antiferromagnetic domains in multiferroic BiFeO_3 films at room temperature. *Nat. Mater.* **5**, 823–829. <https://doi.org/10.1038/nmat1731> (2006).
6. Schlom, D. G. *et al.* Elastic strain engineering of ferroic oxides. *MRS Bull.* **39**, 118–130. <https://doi.org/10.1557/mrs.2014.1> (2014).
7. Ricinschi, D., Yun, K. Y. & Okuyama, M. A mechanism for the 150 μm C cm^{-2} polarization of BiFeO_3 films based on first-principles calculations and new structural data. *J. Phys. Condens. Matter* **18**, 97–105. <https://doi.org/10.1088/0953-8984/18/6/0103> (2006).
8. Dieguez, O., Gonzalez-Vazquez, O. E., Wojdel, J. C. & Iniguez, J. First-principles predictions of low-energy phases of multiferroic BiFeO_3 . *Phys. Rev. B* **83**, 13. <https://doi.org/10.1103/PhysRevB.83.094105> (2011).
9. Xu, G. Y., Li, J. F. & Viehland, D. Ground state monoclinic (M-b) phase in (110)(c) BiFeO_3 epitaxial thin films. *Appl. Phys. Lett.* **89**, 3. <https://doi.org/10.1063/1.2392818> (2006).
10. Zeches, R. J. *et al.* A strain-driven morphotropic phase boundary in BiFeO_3 . *Science* **326**, 977–980. <https://doi.org/10.1126/science.1177046> (2009).
11. Bea, H. *et al.* Evidence for room-temperature multiferroicity in a compound with a giant axial ratio. *Phys. Rev. Lett.* **102**, 5. <https://doi.org/10.1103/PhysRevLett.102.217603> (2009).
12. Chen, Z. H. *et al.* Nanoscale domains in strained epitaxial BiFeO_3 thin films on LaSrAlO_4 substrate. *Appl. Phys. Lett.* **96**, 3. <https://doi.org/10.1063/1.3456729> (2010).
13. Christen, H. M., Nam, J. H., Kim, H. S., Hatt, A. J. & Spaldin, N. A. Stress-induced R-M-A-M-C-T symmetry changes in BiFeO_3 films. *Phys. Rev. B* **83**, 7. <https://doi.org/10.1103/PhysRevB.83.144107> (2011).
14. Liu, H. J., Yang, P., Yao, K. & Wang, J. Growth rate induced monoclinic to tetragonal phase transition in epitaxial BiFeO_3 (001) thin films. *Appl. Phys. Lett.* **98**, 3. <https://doi.org/10.1063/1.3561757> (2011).
15. Yang, J. C. *et al.* Orthorhombic BiFeO_3 . *Phys. Rev. Lett.* **109**, 247606. <https://doi.org/10.1103/PhysRevLett.109.247606> (2012).
16. You, L. *et al.* Domain tuning in mixed-phase BiFeO_3 thin films using vicinal substrates. *Appl. Phys. Lett.* <https://doi.org/10.1063/1.4717986> (2012).
17. Pailloux, F. *et al.* Atomic structure and microstructures of supertetragonal multiferroic BiFeO_3 thin films. *Phys. Rev. B* **89**, 9. <https://doi.org/10.1103/PhysRevB.89.104106> (2014).
18. Bae, I. T. *et al.* Elucidation of crystal and electronic structures within highly strained BiFeO_3 by transmission electron microscopy and first-principles simulation. *Sci. Rep.* **7**, 12. <https://doi.org/10.1038/srep46498> (2017).
19. Kubel, F. & Schmid, H. Structure of a ferroelectric and ferroelastic monodomain crystal of the perovskite BiFeO_3 . *Acta Crystallogr. Sect. B* **46**, 698–702. <https://doi.org/10.1107/S0108768190006887> (1990).
20. Petkov, V. & Shastri, S. Lattice symmetry breaking transition and critical size limit for ferroic orders in nanophase BiFeO_3 . *Phys. Rev. B* **104**, 054121. <https://doi.org/10.1103/PhysRevB.104.054121> (2021).
21. Bae, I.-T., Lingley, Z. R., Foran, B. J., Adams, P. M. & Paik, H. Large bi-axial tensile strain effect in epitaxial BiFeO_3 film grown on single crystal PrScO_3 . *Sci. Rep.* **13**, 19018. <https://doi.org/10.1038/s41598-023-45980-w> (2023).
22. Bae, I. T. & Naganuma, H. Evidence of rhombohedral structure within BiFeO_3 thin film grown on SrTiO_3 . *Appl. Phys. Express* **8**, 4. <https://doi.org/10.7567/apex.8.031501> (2015).
23. Bae, I. T., Naganuma, H., Ichinose, T. & Sato, K. Thickness dependence of crystal and electronic structures within heteroepitaxially grown BiFeO_3 thin films. *Phys. Rev. B* **93**, 6. <https://doi.org/10.1103/PhysRevB.93.064115> (2016).
24. Bae, I. T. *et al.* Tensile stress effect on epitaxial BiFeO_3 thin film grown on KTaO_3 . *Sci. Rep.* **8**, 9. <https://doi.org/10.1038/s41598-018-19487-8> (2018).
25. Bae, I. T. *et al.* Short range biaxial strain relief mechanism within epitaxially grown BiFeO_3 . *Sci. Rep.* **9**, 10. <https://doi.org/10.1038/s41598-019-42998-x> (2019).
26. Ophus, C. Four-dimensional scanning transmission electron microscopy (4D-STEM): From scanning nanodiffraction to ptychography and beyond. *Microsc. Microanal.* **25**, 563–582. <https://doi.org/10.1017/S1431927619000497> (2019).
27. Müller-Caspary, K. & Krause, F. F. Momentum-resolved scanning transmission electron microscopy. In *Encyclopedia of Condensed Matter Physics* 95–108 (Elsevier, 2024).
28. Gesing, T. M., Uecker, R. & Buhl, J.-C. Refinement of the crystal structure of praseodymium orthoscorandate, PrScO_3 . *Zeitschrift für Kristallographie New Crystal Structures* **224**, 365–366. <https://doi.org/10.1524/ncts.2009.0159> (2009).
29. Williams, D. B. B. & Carter, C. B. *Transmission Electron Microscopy* 2nd edn. (Springer, 2009).
30. Müller, K. *et al.* Atomic electric fields revealed by a quantum mechanical approach to electron picodiffraction. *Nat. Commun.* **5**, 5653. <https://doi.org/10.1038/ncomms6653> (2014).
31. Shibata, N. *et al.* Electric field imaging of single atoms. *Nat. Commun.* **8**, 15631. <https://doi.org/10.1038/ncomms15631> (2017).
32. Addiego, C., Gao, W. & Pan, X. Thickness and defocus dependence of inter-atomic electric fields measured by scanning diffraction. *Ultramicroscopy* **208**, 112850. <https://doi.org/10.1016/j.ultramic.2019.112850> (2020).
33. Mukherjee, D. *et al.* 4D-STEM differential phase contrast microscopy across ferroelectric domain walls. *Microsc. Microanal.* **24**, 228–229. <https://doi.org/10.1017/s1431927618001630> (2018).
34. Yadav, A. K. *et al.* Spatially resolved steady-state negative capacitance. *Nature* **565**, 468–471. <https://doi.org/10.1038/s41586-018-0855-y> (2019).

35. Park, T.-J. *et al.* Electronic structure and chemistry of iron-based metal oxide nanostructured materials: A NEXAFS investigation of BiFeO_3 , $\text{Bi}_2\text{Fe}_4\text{O}_9$, $\alpha\text{-Fe}_2\text{O}_3$, $\gamma\text{-Fe}_2\text{O}_3$, and $\text{Fe/Fe}_3\text{O}_4$. *J. Phys. Chem. C* **112**, 10359–10369. <https://doi.org/10.1021/jp801449p> (2008).
36. Rossell, M. D. *et al.* Atomic structure of highly strained BiFeO_3 thin films. *Phys. Rev. Lett.* **108**, 5. <https://doi.org/10.1103/PhysRevLett.108.047601> (2012).
37. Sæterli, R., Selbach, S. M., Ravindran, P., Grande, T. & Holmestad, R. Electronic structure of multiferroic BiFeO_3 and related compounds: Electron energy loss spectroscopy and density functional study. *Phys. Rev. B* **82**, 064102. <https://doi.org/10.1103/PhysRevB.82.064102> (2010).
38. Kim, Y. H., Bhatnagar, A., Pippel, E., Alexe, M. & Hesse, D. Microstructure of highly strained BiFeO_3 thin films: Transmission electron microscopy and electron-energy loss spectroscopy studies. *J. Appl. Phys.* <https://doi.org/10.1063/1.4863778> (2014).
39. Chen, Z. H. *et al.* Large tensile-strain-induced monoclinic M-B phase in BiFeO_3 epitaxial thin films on a PrScO_3 substrate. *Phys. Rev. B* **88**, 6. <https://doi.org/10.1103/PhysRevB.88.054114> (2013).
40. Chen, Z. H. *et al.* Low-symmetry monoclinic phases and polarization rotation path mediated by epitaxial strain in multiferroic BiFeO_3 thin films. *Adv. Funct. Mater.* **21**, 133–138. <https://doi.org/10.1002/adfm.201001867> (2011).
41. Bae, I. T. *et al.* Strategy to utilize transmission electron microscopy and X-ray diffraction to investigate biaxial strain effect in epitaxial BiFeO_3 films. *Jpn. J. Appl. Phys.* **57**, 12. <https://doi.org/10.7567/jjap.57.0902a5> (2018).
42. Jang, H. W. *et al.* Strain-induced polarization rotation in epitaxial (001) BiFeO_3 Thin Films. *Phys. Rev. Lett.* **101**, 107602. <https://doi.org/10.1103/PhysRevLett.101.107602> (2008).
43. Bae, I. T. *et al.* Growth mechanism and domain structure study on epitaxial BiFeO_3 film grown on $(\text{La}_{0.3}\text{Sr}_{0.7})(\text{Al}_{0.65}\text{Ta}_{0.35})\text{O}_3$. *J. Appl. Phys.* **127**, 8. <https://doi.org/10.1063/5.0005672> (2020).
44. Han, M. J. *et al.* Mapping gradient-driven morphological phase transition at the conductive domain walls of strained multiferroic films. *Phys. Rev. B* **100**, 104109. <https://doi.org/10.1103/PhysRevB.100.104109> (2019).
45. Das, G. & Mitchell, T. E. Electron irradiation damage in quartz. *Radiat. Effects* **23**, 49–52. <https://doi.org/10.1080/00337577408232044> (1974).
46. Ishimaru, M., Bae, I.-T. & Hirotsu, Y. Electron-beam-induced amorphization in SiC . *Phys. Rev. B* **68**, 144102. <https://doi.org/10.1103/PhysRevB.68.144102> (2003).
47. Williams, D. B. & Carter, C. B. *Transmission Electron Microscopy* 2nd edn. (Springer, 2009).
48. Shimada, T. *et al.* Multiferroic nature of intrinsic point defects in BiFeO_3 : A hybrid Hartree-Fock density functional study. *Phys. Rev. B* **93**, 174107. <https://doi.org/10.1103/PhysRevB.93.174107> (2016).
49. Geneste, G., Paillard, C. & Dkhil, B. Polaron, vacancies, vacancy associations, and defect states in multiferroic BiFeO_3 . *Phys. Rev. B* **99**, 024104. <https://doi.org/10.1103/PhysRevB.99.024104> (2019).
50. Bae, I.-T., Ishimaru, M. & Hirotsu, Y. Structural changes of SiC under electron-beam irradiation: Temperature dependence. *Nucl. Instrum. Methods Phys. Res. Sect. B Beam Interact. Mater. Atoms* **250**, 315–319. <https://doi.org/10.1016/j.nimb.2006.04.130> (2006).
51. Chakravadhanula, V. S. K. *et al.* Electron beam effects on oxide thin films—Structure and electrical property correlations. *Microsc. Microanal.* **25**, 592–600. <https://doi.org/10.1017/S1431927619000175> (2019).

Acknowledgements

This work was partially funded by Aerospace Technical Investment Program (No. 801604) from The Aerospace Corporation. This work made use of Thin Film Growth Facility of the Platform for the Accelerated Realization, Analysis, and Discovery of Interface Materials (PARADIM), which is supported by the National Science Foundation under Cooperative Agreement No. DMR-2039380.

Author contributions

I.T.B., and H.P. conceived the study. H.P. deposited the film. I.T.B., and B.J.F. performed F.I.B. and T.E.M. I.T.B. wrote the manuscript with inputs from all authors. All authors have given approval to the final version of the manuscript.

Competing interests

The authors declare no competing interests.

Additional information

Supplementary Information The online version contains supplementary material available at <https://doi.org/10.1038/s41598-024-66382-6>.

Correspondence and requests for materials should be addressed to I.-T.B.

Reprints and permissions information is available at www.nature.com/reprints.

Publisher's note Springer Nature remains neutral with regard to jurisdictional claims in published maps and institutional affiliations.



Open Access This article is licensed under a Creative Commons Attribution 4.0 International License, which permits use, sharing, adaptation, distribution and reproduction in any medium or format, as long as you give appropriate credit to the original author(s) and the source, provide a link to the Creative Commons licence, and indicate if changes were made. The images or other third party material in this article are included in the article's Creative Commons licence, unless indicated otherwise in a credit line to the material. If material is not included in the article's Creative Commons licence and your intended use is not permitted by statutory regulation or exceeds the permitted use, you will need to obtain permission directly from the copyright holder. To view a copy of this licence, visit <http://creativecommons.org/licenses/by/4.0/>.

© The Author(s) 2024